

Numerical and experimental investigation of the metering characteristic and pressure losses of the rotary tubular spool valve.

Ivan Okhotnikov^{a,b,*}, Karem Abuowda^a, Siamak Noroozi^a, Philip Godfrey

^a*Department of Design and Engineering, Faculty of Science and Technology, Bournemouth University, Poole House, Talbot Campus, Fern Barrow, Poole, Dorset, BH12 5BB, United Kingdom*

^b*Hydreco Hydraulics Limited, 32 Factory Road, Poole, Dorset, BH16 5SL, United Kingdom*

Abstract

This paper presents the results of numerical and experimental performance evaluation of the rotary tubular spool valve. The aim of this work is to develop further the novel design of the tubular spool valve by confirming experimentally the validity of the simulation model and its results, thereby proving the valve's potential to represent a feasible and more efficient alternative to conventionally used translation spool valves avoiding the use of two stage valve configurations. In this research the valve performance is assessed through numerical modelling and experimental studies of its metering characteristic and pressure losses. This paper demonstrates that the used valve model yields the results, which agree well with the conducted experimental study. Therefore, validation of the numerical model and the modelling results in the form of theoretical valve characteristics was accomplished. Firstly, the paper presents details of a numerical approach employed to evaluate valve performance and then analyzes the simulation results. Next, the valve performance is experimentally validated by testing a prototype valve on a hydraulic test rig capable of measuring the volume flow rate, pressure levels in up- and downstream lines of the valve across the entire spool angular stroke. Initially, average discrepancies between modelling and test results were 52.46% for the metering and 82.78% for the pressure loss characteristics. Correcting the model geometry aimed at eliminating differences between the valve model and the practically used prototype-test rig system enabled reduction of the error between experiment and modelling by 47.75% for the pressure loss function. This confirmed validity of the simulated characteristics of the valve. The benchmark comparison of pressure losses confirmed average 71.66% energy dissipation reduction compared to the industry-available analogue valve.

Keywords:

Computational fluid dynamics, experiment, validation, valve

1. Introduction

Fluid power offers a series of advantages unavailable to other drives, especially in applications requiring significant mechanical power output. Among the assets are high power density, reliability and a lower operating cost compared to competing technologies. Power hydraulics has a wide operating bandwidth. That enables fast starts, stops, and reversals. Working fluid in these systems performs power transmitting, lubricating and heat averting functions [1]. Moreover,

due to the large bulk modulus of hydraulic mineral oil, a fluid power drive is less sensitive to impact loads, provides natural damping and, thus, is more reliable than mechanical transmissions [2]. These factors have made hydraulics indispensable for high power applications and ensured its dominance among power drive technologies.

*Corresponding author

Email addresses: iokhotnikov@bournemouth.ac.uk (Ivan Okhotnikov), kabuowda@bournemouth.ac.uk (Karem Abuowda), snoroozi@bournemouth.ac.uk (Siamak Noroozi), pd.godfrey@ntlworld.com (Philip Godfrey)

Nomenclature**Latin**

A	Area, mm ²
A_v	Van Driest coefficient
C_d	Discharge coefficient
$C_{\varepsilon 1}, C_{\varepsilon 2}, C_{\mu}, C_B$	Constants in the k - ε model
d, D	Diameter, mm
D_h	Hydraulic diameter, mm ²
f_1, f_2, f_{μ}	Lam and Bremhost's damping functions in k - ε turbulence model
F	Force, N
k	Turbulent kinetic energy, m ² s ⁻²
K	Karman constant
l, L	Length, characteristic length, mm
p	Pressure, MPa
P	Power, W
Q	Volume flow rate, L min ⁻¹
R_T, R_y	Turbulence and velocity-average Reynolds number
Re	Reynolds number
S	Perimeter, mm
t	Time, s
u_i	The i -th component of the fluid velocity vector, m s ⁻¹
u^+	Dimensionless longitudinal velocity
v, V	Average, characteristic velocity, m s ⁻¹
y	Distance from the wall surface, m
y^+	Dimensionless wall distance
x_i	The i -th component of the coordinate vector, m

Greek

δ_{ij}	Kronecker function
ε	Turbulent dissipation rate, m ² s ⁻² , strain
μ	Dynamics viscosity, Pa s
μ_t	Turbulent eddy viscosity coefficient
ν	Kinematic viscosity, m ² s ⁻¹
ρ	Density, kg m ⁻³
$\sigma_k, \sigma_{\varepsilon}, \sigma_B$	Constants in the k - ε model
τ_{ij}	Reynolds stress tensor, MPa
τ_w	Wall shear stress, MPa
ϕ	Spool angular position, °

Notation \bar{x} Mean value of x **Acronyms**

AEM	Asynchronous Electric Motor
CAD	Computer Aided Design
CFD	Computational Fluid Dynamics
DAS	Data Acquisition System
FM	Flow Meter
PRV	Pressure Relief valve
PT	Pressure Transducer
RTSV	Rotary Tubular Spool Valve
SM	Stepper Motor
TT	Torque Transducer
VAC	Volts of Alternating Current
VDC	Volts of Direct Current
VFD	Variable-Frequency Drive

19

20

21 However, fluid power possesses several drawbacks.
 22 Tight clearances between mechanical parts require
 23 extremely clean working fluid free from solid particles,
 24 dissolved gasses and air. It necessitates regular and
 25 strict supervision of the oil's contamination level during
 26 an exploitation period. Other shortcomings are low
 27 flexibility and high non-linearity of hydraulic control
 28 relative to electromagnetic counterparts [1]. Hydraulics
 29 is also prone to oil leakage through seals, mechanical
 30 contacts and connections [3], which can cause spillages
 31 and environmental pollution.

32 The presence of valves modulating the output velocity
 33 of the hydraulic actuator remains the main design
 34 feature of the state of the art power hydraulic systems
 35 due to robustness and a relatively low cost of this
 36 solution [4]. Flow- and pressure-regulating valves
 37 enable a link between the source of hydraulic power and
 38 its consumers, implement complex logic of actuators
 39 operation in a working cycle. The actuator's speed
 40 regulation is fulfilled through throttling adjustment,
 41 which realized by changing the valve's spool position.
 42 The spool position determines an orifice area, which in
 43 turn defines valve's hydraulic resistance. The flow rate
 44 to the actuator as well as its output velocity changes
 45 according to this area.

46 The common trait of valve-controlled systems is
 47 prevalence of throttling losses due to a resistive
 48 nature of flow regulation. Since the flow regulation
 49 is being fulfilled by restraining the flow inside the
 50 valve, excessive fluid power is dissipated in a form
 51 of vortices with substantial viscous friction losses
 52 and heat generation in them. These result in poor
 53 energy efficiency of the valve as well as the entire
 54 hydraulic system it is installed in. The review of the
 55 industrial state-of-the-art and research advancements in

56 development of direct drive proportional spool valves 106
57 [5] confirms optimization of the flow paths through the 107
58 valve to lessen flow disturbances is viable, well known 108
59 and tested technique to solve efficiency issues in valves 109
60 and reduce pressure losses. 110

61 Judging by flow streamlines in the conventionally used 111
62 spool and seat valves obtained through visualization of 112
63 flow paths with CFD [6], [7], it has been concluded 113
64 that, firstly, exact geometry of the valve is a sole factor 114
65 defining flow trajectories, pressure losses and hence 115
66 efficiency of the valve; secondly, streamlining flow 116
67 paths is a way to improve valve efficiency and to reduce 117
68 flow forces on a spool [8]; and finally, the easiest way 118
69 to implement streamlining is to remove unnecessary 119
70 turns and sudden cross-sectional changes of flow paths,
71 which are in abundance in linear spool valves. The
72 most obvious way to keep the flow route smooth is
73 to rid of sudden U-turns. These considerations let to
74 infer that rotary valves could provide more streamlined
75 flow trajectories and ease of valve operation. Unlike
76 conventional linear spool configurations, a rotating
77 spool design especially with a hollow spool would
78 create a much smaller net area of surfaces subjected to
79 the flow forces, hence decreasing power consumption of
80 a valve driving mechanism.

81 So far, the employment of rotary spools industrially 128
82 is limited to manually driven on-off ball valves, flow 129
83 dividers, plug and steering valves, which are used in the 130
84 steering systems of wheeled vehicles [9]. In the rotary 131
85 ball valves, usually a rotary spool is spherical in a cross 132
86 section with drilled through-holes serving as flow paths. 133
87 In valves with cylindrical spools, flow paths are milled 134
88 on the external cylinder of the spool, imposing sudden 135
89 changes in direction and a cross sections of flow paths. 136
90 Although these valve structures still include undesirable 137
91 U-turns in flow trajectories [10], the required effort to 138
92 operate them is comparable with currently used linear 139
93 sliding spools [11], their dynamic performance is also 140
94 similar to conventional linear spools [12], [13]. 141

95 Among multitude patents dedicated to the rotary valve 142
96 structures, there are design solutions suggesting a 143
97 tubular spool as the main throttling part. Embodying 144
98 the approach of mobile surfaces minimization and 145
99 using rotary control motion, these concepts represent 146
100 a promising and under-studied class of control valve 147
101 designs suitable for high-power hydraulics applications. 148
102 The first found patents proposing such structures were 149
103 filed in the middle of the last century by Husley and 150
104 Erwin as rotary sleeve valves [14] and [15]. 151

105 The present research aims at validating the used 152

methodology to obtain CFD simulated performance 106
characteristics of the previously suggested design 107
of the rotary tubular valve, thereby, confirming 108
its flow controlling capabilities and potential to 109
improve controllability and energy efficiency of spool 110
valves. Experimental validation was employed 111
to investigate flow forces and pressure drop in 112
conventional directional control valves [16], to explore 113
performance of innovative designs of linear spools [17] 114
as well as rotary valves [18]. Overall, these would 115
allow to develop further this promising design and to 116
prove that the rotary spool valve is a viable competitor 117
to conventional linear spool valves in terms of metering 118
capabilities and energy efficiency. 119

120 2. Rotary tubular spool valve

121 2.1. Design

122 The design of the rotary tubular spool valve (RTSV) 123
and theoretical analysis of flow physics within it have 124
been reported in details in the authors' previous work 125
[19]. The current research investigates the same valve 126
structure, although the down scaled version, which 127
had enabled experiments on a test rig described in the 128
following sections.

129 The cut section in fig. 1 illustrates the RTSV design 130
and operation. The oil enters the RTSV through the 131
circular inlet area A_{in} . Then, it flows into the central 132
chamber of the spool 1. The chamber is formed by 133
spool's internal cylindrical and conical surfaces and the 134
circular area A_1 . From the central chamber the oil 135
passes through two throttling orifices, which are created 136
by overlapping openings on the spool 1 and the sleeve 137
2, see fig. 1. Next, the oil finds its way from the orifices 138
to the annular oil collecting channel, or chamber, with 139
the cross-sectional area of A_{an} , which encircles the 140
sleeve. The collecting chamber is connected to the 141
outlet hydraulic port with the circular area A_{out} , which 142
is designed to be equal to A_{in} .

143 To keep hydraulic disturbances to the flow as small as 144
possible, the cross-sectional area of the entering flow 145
 A_{in} should be maintained throughout valve's internal 146
passages up to the exit port with the area A_{out} . This 147
approach results in the design criterion for selecting 148
cross-sectional areas of the valve's channels.

149 Since there are two throttling orifices on the spool and 150
the total flow is split in two jets, the annular area of the 151
flow in the collecting chamber A_{an} needs to be equal to 152
a half of the inlet flow's cross-sectional area A_{in} , i.e.

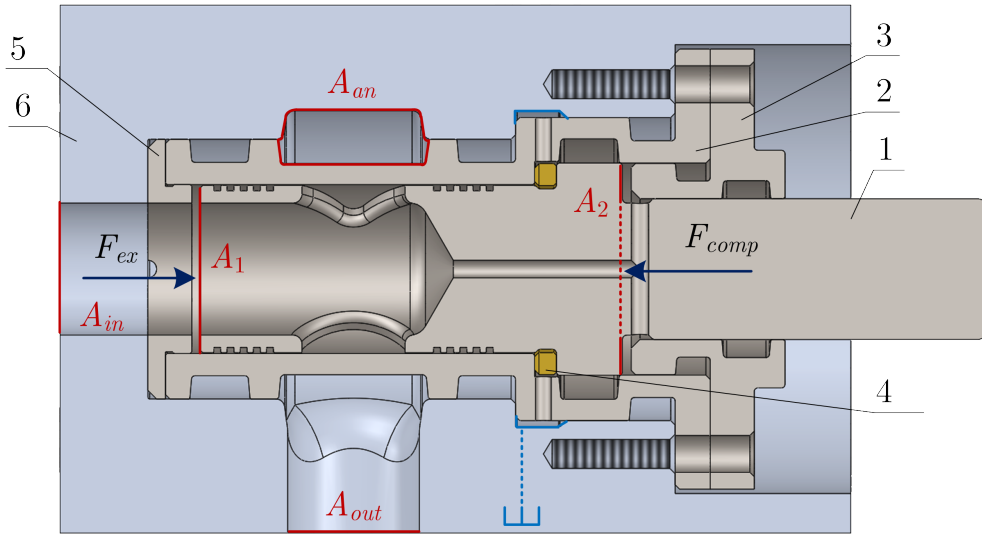


Figure 1: The cutaway section of the RTSV. Original parts: 1 – spool, 2 – sleeve, 3 – lid, 4 – thrust bearing, 5 – guiding sleeve, 6 – valve body. The region inside the spool to the right of the area A_1 – the spool central chamber or cavity. The annular region with the cross section of A_{an} – the cross-section of the single branch of the collecting channel or chamber. A_{in} and A_{out} – inlet, supply and outlet, service ports respectively. A_2 – the annular area of the spool back, or compensating chamber.

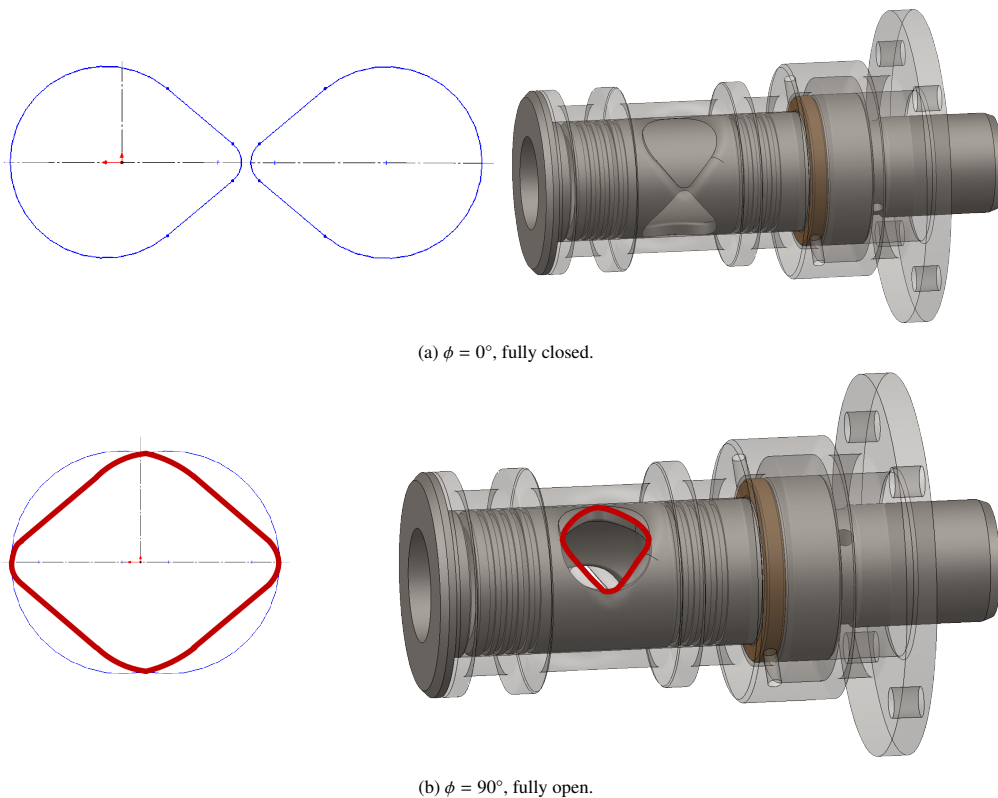


Figure 2: The single throttling orifice at the extreme states. Left – overlap of the unfolded throttling profiles of the spool and sleeve openings. Right – location of the single throttling orifice on the spool-sleeve assembly.

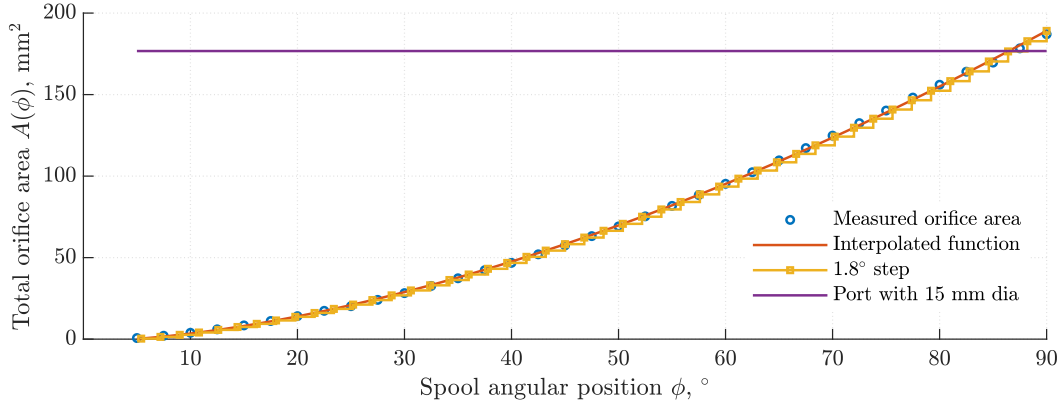


Figure 3: The total orifice area function, $A(\phi)$.

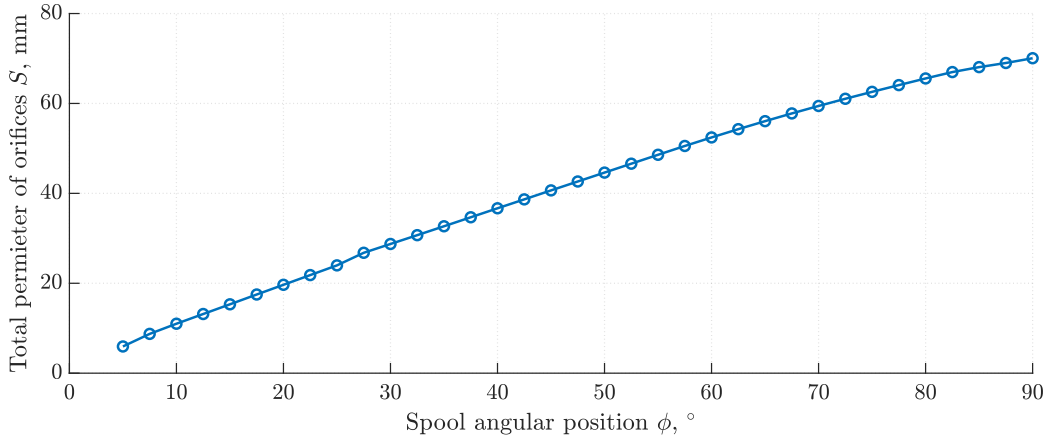


Figure 4: Total perimeter of the throttling orifices, $S(\phi)$.

$$A_{in} = A_{out} = 2A_{an}. \quad (1)$$

153 At any moment the tubular spool is exposed to the pump
 154 pressure p_p acting on the spool's circular surface A_1 .
 155 This creates the extruding force F_{ex} that pushes the
 156 spool out from the valve body.

$$F_{ex} = p_p A_1 \quad (2)$$

157 To compensate this force and to locate the spool in a
 158 certain axial position, the oil is directed through the
 159 axial channel inside the the spool to its back chamber.
 160 There, the oil acts on the annular area A_2 with the
 161 pump pressure p_p , which creates the compensating
 162 force F_{comp} .

$$F_{comp} = p_p A_2 \quad (3)$$

163 Therefore, assuming pressure levels are equal in the
 164 spool central and the back chambers, the design
 165 criterion for selecting areas A_1 and A_2 as well as
 166 ensuring spool axial stabilization is

$$\begin{aligned} F_{comp} &\geq F_{ex} \\ A_2 &\geq A_1 \end{aligned} \quad (4)$$

167 If the annular area A_2 exceeds the circular area A_1 ,
 168 the compensating force surpasses the ejecting force, i.e.
 169 $F_{comp} > F_{ex}$. In this case, the spool is pushed against the
 170 brass thrust bearing 4 in fig. 1. The bearing's material
 171 needs to ensure a low friction pair between the steel or
 172 aluminum spool and the bearing.

173 The thrust bearing features radial grooves to allow the
 174 oil leakage from the spool-sleeve clearance to drain to
 175 the tank. In fig. 1 the groove, which is cut in the body 6

176 and is outlined in blue, collects this leakage and drains 225
 177 it to the tank. The drainage channel also collects the
 178 oil flowing from the spool back chamber through the 226
 179 sleeve's groove of the sealing rings. Combined internal 227
 180 leakage from these two paths enables hydrodynamic 228
 181 bearing on spool and thrust bearing mating surfaces. 229

182 The guiding sleeve 5 serves to facilitate dismantling of 230
 183 the valve in case replacement of any internal parts is 231
 184 needed. Semi-circular cuts on the sleeve bottom plane 232
 185 can be used to pull all valve inner parts from the body 6. 233
 186 The lid 3 ensures all immovable parts are securely fixed 234
 187 by tightening screw fasteners to designated threaded 235
 188 blind holes on the housing 6.

189 2.2. Operation

190 The throttling pair in fig. 2 performs regulation of the 236
 191 flow area and, hence, the flow rate passing through 237
 192 the RTSV. The flow rate is directly proportional to the 238
 193 overlap area between the slots of the rotary actuated 239
 194 spool and the static sleeve. The total area of the 240
 195 throttling orifices varies in a range between the fully 241
 196 closed and full open states shown in figs. 2a and 2b 242
 197 respectively. Therefore, the angular position of the 243
 198 spool ϕ in the sleeve defines the openings' overlap, the 244
 199 total orifice area A and the resultant oil's flow rate Q . 245

200 The total orifice area is also a function of each window 246
 201 profile. In the current research, the shape of openings 247
 202 was chosen to be the same for the spool and the sleeve, 248
 203 with areas chosen according to above mentioned design 249
 204 criteria, i.e. the maximum total orifices area at the fully 250
 205 open state is designed to be as close as possible to the 251
 206 inlet flow cross section ensuring the least resistance to 252
 207 the flow.

208 The openings on the sleeve and the spool form the 253
 209 orifice with the total opening area function $A(\phi)$ shown 254
 210 in fig. 3. The increase of the area is nonlinear with 255
 211 a more gradual increment at lower angles of opening.
 212 The slow non-linear change in the area at the start
 213 of actuation is a special design feature of the RTSV.
 214 The dependency at $\phi > 50^\circ$ of the spool angular
 215 position is steeper, reaching the total orifice opening of
 216 186.99 mm^2 . The graph also includes the area of the
 217 hydraulic inlet port with the diameter of 15 mm, which
 218 results in the inlet flow cross section of 176.71 mm^2 .
 219 The step-wise line in fig. 3 illustrates the area increase
 220 in the case the spool position is defined with a
 221 conventional stepper motor with 1.8° step. Additionally,
 222 the orifices's perimeter was measured, see fig. 4, to
 223 enable Reynolds number estimation in the following
 224 section.

225 3. CFD modelling

226 3.1. Turbulence model

227 In the intended application of the RTSV, which is
 228 high pressures and high flow rates, the fluid flow
 229 inside the valve tends to be turbulent. In the
 230 used CAD-embedded CFD software, FloEFD suit,
 231 the Favre-averaged Navier-Stokes equations are used,
 232 where the effects of the flow turbulence on the
 233 mass-averaged flow parameters are considered. The
 234 applied Favre averaging method also accounts for
 235 fluctuations of fluid density and temperature [20].

236 To close the system of Navier-Stokes equations,
 237 transport equations for the turbulent kinetic energy
 238 and its dissipation rate are employed, the so-called
 239 k - ε model [21]. The adopted model meets accuracy
 240 and reliability requirements in the considered valve
 241 study and performs satisfactorily in solving fluid power
 242 problems [22].

243 In FloEFD the classical two-equations k - ε empirical
 244 model for simulating turbulence in fluid flow is used
 245 as it requires the minimum amount of additional
 246 information to define the flow [23]. The modified
 247 k - ε turbulence model with damping functions [24]
 248 describes laminar, turbulent, and transitional flows
 249 of homogeneous fluids consisting of the following
 250 turbulence conservation laws [20], [25]:

$$\frac{\partial \rho k}{\partial t} + \frac{\partial \rho k u_i}{\partial x_i} = \frac{\partial}{\partial x_i} \left(\left(\mu + \frac{\mu_t}{\sigma_k} \right) \frac{\partial k}{\partial x_i} \right) + \tau_{ij}^R - \rho \varepsilon + \mu_t P_B \quad (5)$$

$$\frac{\partial \rho \varepsilon}{\partial t} + \frac{\partial \rho \varepsilon u_i}{\partial x_i} = \frac{\partial}{\partial x_i} \left(\left(\mu + \frac{\mu_t}{\sigma_\varepsilon} \right) \frac{\partial \varepsilon}{\partial x_i} \right) + C_{\varepsilon 1} \frac{\varepsilon}{k} \left(f_1 \tau_{ij}^R \frac{\partial u_i}{\partial x_j} + C_B \mu_t P_B \right) - f_2 C_{\varepsilon 2} \frac{\rho \varepsilon^2}{k} \quad (6)$$

251 Here P_B represents turbulence generation due to
 252 buoyancy and can be written as

$$P_B = - \frac{g_i}{\rho \sigma_B} \frac{\partial \rho}{\partial x_i}, \quad (7)$$

253 where g_i is the component of gravitational acceleration
 254 in direction of x_i . The empirical k - ε constants have the
 255 following typical values [21]: $\sigma_k = 1$, $\sigma_B = 0.9$, $\sigma_\varepsilon =$

256 1.3, $C_\mu = 0.09$, $C_{\varepsilon 1} = 1.44$, $C_{\varepsilon 2} = 1.92$ and constant
 257 $C_B = 1$ if $P_B > 0$, and 0 otherwise.

258 Following Boussinesq assumption, the Reynolds-stress
 259 tensor for Newtonian fluids has the following form:

$$\tau_{ij}^R = \mu \left(\frac{\partial u_i}{\partial x_j} + \frac{\partial u_j}{\partial x_i} - \frac{2}{3} \delta_{ij} \frac{\partial u_k}{\partial x_k} \right) - \frac{2}{3} \delta_{ij} \rho k. \quad (8)$$

260 Here δ_{ij} is the Kronecker delta function (it is equal to
 261 unity when $i = j$, and zero otherwise), μ is the dynamic
 262 viscosity coefficient, k is the turbulent kinetic energy
 263 and μ_t is the turbulent eddy viscosity coefficient, which
 264 is determined from

$$\mu_t = \frac{f_\mu C_\mu \rho k^2}{\varepsilon}. \quad (9)$$

265 Here f_μ is the turbulent viscosity factor. It is determined
 266 by the expression

$$f_\mu = \left(1 - e^{-0.0165R_y} \right)^2 \left(1 + \frac{20.5}{R_T} \right), \quad (10)$$

$$R_y = \frac{\rho \sqrt{ky}}{\mu}, \quad (11)$$

$$R_T = \frac{\rho k^2}{\mu \varepsilon} \quad (12)$$

267 Lam and Bremhorst's damping functions f_μ , f_1 , f_2
 268 decrease turbulent viscosity and turbulence energy
 269 and increase the turbulence dissipation rate when the
 270 Reynolds number R_y , based on the average velocity of
 271 fluctuations and distance from the wall becomes too
 272 small. When $f_\mu = 1$, $f_1 = 1$, $f_2 = 1$ the approach
 273 obtains the original k - ε model.

274 3.2. Wall function

275 To simulate fluid boundary layer effects near solids
 276 within the k - ε model a "two-scale wall function"
 277 approach [26] is utilized. The FloEFD employs Van
 278 Driest's profiles [27].

279 When the number of fluid cells across the boundary
 280 layer more than 10, modelling of a laminar boundary
 281 layer is done via Navier-Stokes equations as part of
 282 the core flow calculation. For turbulent boundary
 283 layers proceeding from the Van Driest mixing length
 284 [27], the FloEFD uses following dependency of
 285 the dimensionless longitudinal velocity u^+ on the
 286 dimensionless wall distance y^+ [23]

$$u^+ = \frac{u}{\sqrt{\frac{\tau_w}{\rho}}} = \int_0^{y^+} \frac{2d\eta}{1 + \sqrt{1 + 4K^2\eta^2(1 - e^{-\frac{\eta}{A_v}})^2}}. \quad (13)$$

287 Here $K = 0.4504$ is the Karman constant and the Van
 288 Driest coefficient is $A_v = 26$.

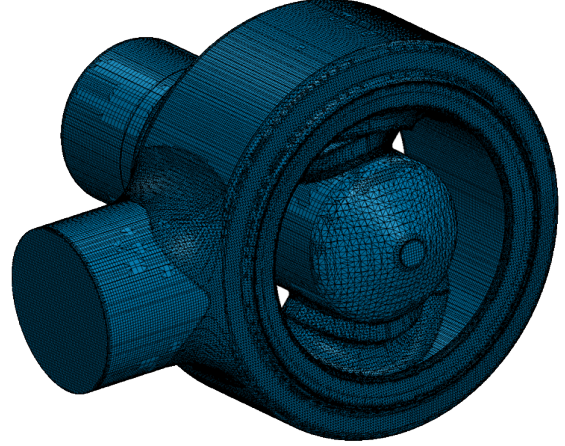


Figure 5: The mesh of the fluid subdomain with ≈ 1 million fluid cells.

289 3.3. Mesh

290 The fluid subdomain was extracted from the three
 291 dimensional geometric model of the RTSV. Then, the
 292 fluid domain was split into cells with adjustable
 293 resolution. The governing partial differential
 294 Navier-Stokes and transport equations were solved in
 295 nodes, in centres of the mesh cells. The FloEFD solves
 296 the governing equations with a discrete numerical
 297 technique based on the finite volume discretization
 298 method.

299 Meshing in the FloEFD results in rectangular
 300 parallelepiped cells with orthogonal faces, see fig. 5.
 301 The near-boundary cells are fractions of the original
 302 cells that are cut by the solid matter geometry boundary.
 303 Thus, the resulting near-boundary cells are polyhedrons
 304 with both axis-oriented and arbitrary oriented plane
 305 faces, partial cells. All physical and inertial parameters
 306 are referred to the mass centres of the cells within the
 307 control volume [21].

308 The module uses the immersed body meshing approach,
 309 which provides the structured Cartesian mesh with an
 310 irregular distribution of the mesh cells, which speeds up
 311 the search for data associated with neighbour cells and
 312 has been shown to deliver the lowest local truncation
 313 error. The approach also simplifies navigation on

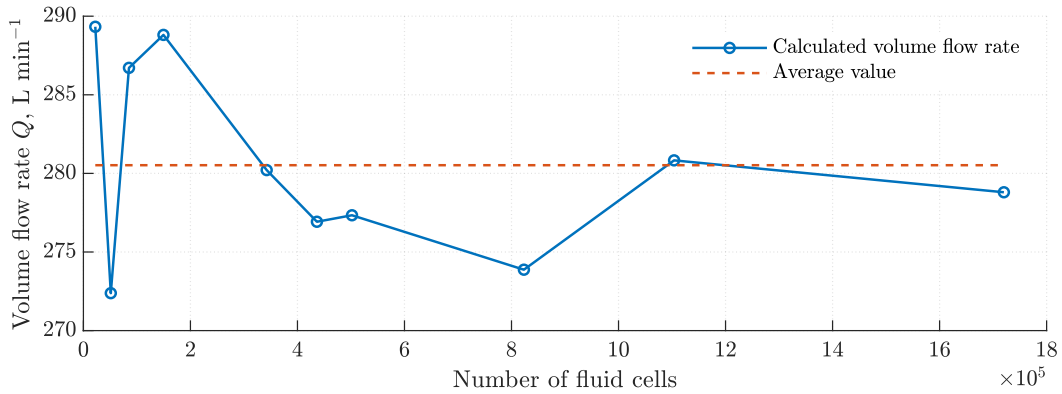


Figure 6: Grid independence study results. The mean value $\bar{Q} = 280.46 \text{ L min}^{-1}$, the standard deviation $\sigma = 5.97 \text{ L min}^{-1}$, which is 2.13% deviation from the mean value.

314 the mesh and to ensure robustness of the differencing
 315 scheme by the absence of secondary skewed faces [28].
 316 Applied solution-adaptive refinement process allows
 317 further splitting the mesh cells the high-gradient
 318 flow regions, which cannot be resolved prior to
 319 the calculation and merging the mesh cells in the
 320 low-gradient regions. It serves to minimize the spatial
 321 error arising from the discretization of the governing
 322 differential equations [28].

3.3.1. Grid independence

323 A grid independence analysis has been performed for
 324 the case of $\Delta p = 1 \text{ MPa}$ pressure drop between
 325 up- and downstream openings of the valve and the
 326 spool angular position $\phi = 90^\circ$ corresponding to the
 327 full open state. For these conditions, several meshes
 328 were created differing in a number of fluid cells from
 329 22 000 to 1 700 000. The mean value of the computed
 330 flow rate between different meshes is equal to $\bar{Q} =$
 331 $280.46 \text{ L min}^{-1}$ with 2.13% fluctuations of the extreme
 332 values around the average one.
 333

334 The standard deviation is 5.97 L min^{-1} , which is
 335 considered as an acceptable value to conclude that
 336 the obtained values ensure the convergence of the
 337 solution regardless of the mesh resolution. The applied
 338 mesh resolutions provide acceptable accuracy of the
 339 computed results. The result of the mesh independence
 340 study is shown in fig. 6.

341 The meshing for further parametric studies was selected
 342 such that it provides on average 1.1 million fluid cells
 343 and 3 million partial cells on the surfaces bordering with
 344 solid matter. The maximum cell size of the basic mesh
 345 before the refinement process commences is 0.8 mm.

346 The chosen meshing setting guarantees a reasonable
 347 trade-off between computational time and accuracy for
 348 the simulations described further.

3.4. Boundary conditions

349 The specification of the boundary conditions consists of
 350 assigning the desired magnitude of the flow parameters
 351 to the fluid subdomain's openings and establishes the
 352 hydraulic problem to be solved by the FloEFD. In
 353 this study, a wall roughness and slip conditions were
 354 not imposed, there were no leakages through external
 355 sealing lids of the valve's fluid domain.
 356

357 The first objective is to model metering performance
 358 of the valve by quantifying the valve's discharge
 359 coefficient $C_d(\phi)$ and the metering function $Q(\phi)$.
 360 In these parametric simulations, Dirichlet boundary
 361 conditions for the stationary turbulent fluid flow were
 362 used. Namely, boundary conditions for the valve
 363 inlet were selected as the static pressure of $p_{in} =$
 364 0.35 MPa , 0.6 MPa and 1.1 MPa . The valve outlet
 365 opening was subjected to the invariant static pressure
 366 of $p_{out} = 0.1 \text{ MPa}$ corresponding to a pressure level of
 367 the "breathing" oil tank.

368 Thus, the boundary condition of the adopted pressure
 369 drop makes up a set of $\Delta p = 0.25 \text{ MPa}$, 0.5 MPa and
 370 1 MPa pressure differentials. The magnitudes of the
 371 pressure differential were selected according to an usual
 372 margin of pressure levels in load sensing systems, which
 373 is in a range 10 bar to 20 bar [29], [30].

374 This set of hydraulic boundary conditions provided
 375 varying values of the pressure difference Δp , dictating
 376 the volume flow rate Q passing through the orifice.
 377 For each variation of the specified input, the angular

Simulation type	Internal stationary turbulent flow simulation
Geometric model	Discrete spool openings $\phi = 10^\circ$ to 90° with 5° step
Fluid model	Single-phase flow, mineral hydraulic oil ISO VG 32 at 45°C <ul style="list-style-type: none"> • $\rho = 850 \text{ kg m}^{-3}$ • $\nu = 29 \text{ cSt}$, • $\mu = 24.68 \text{ cP}$
Mesh	Adaptive finite volume discretization, rectangular parallelepipeds with initial maximum size 0.8 mm , number of cells ≈ 1.1 million
Turbulence model	k - ε turbulence model
Boundary conditions	Metering characteristic Static pressure at the inlet and the outlet: <ul style="list-style-type: none"> • $p_{in} = 0.35 \text{ MPa}$, 0.6 MPa and 1.1 MPa • $p_{out} = 0.1 \text{ MPa}$ Power loss characteristic: Volume flow rates across the RTSV: <ul style="list-style-type: none"> • $Q = 25 \text{ L min}^{-1}$ to 275 L min^{-1} with the 25 L min^{-1} increment Other simulation conditions: <ul style="list-style-type: none"> • No-slip, smooth, adiabatic wall • Two-scale wall function • Turbulence intensity 2% • Turbulence length 0.1 mm • Leakages in clearances are neglected

Table 1: Preprocessing settings of the CFD modelling.

378 position of the spool ϕ was added as the geometrical
379 parameter varying from 10° to full open state of 90°
380 with a 5° step.

381 Secondly, the pressure loss p_{loss} was modeled by
382 varying a valve inlet volume flow rate within a range
383 Q 25 L min^{-1} to 275 L min^{-1} coupled with the invariant
384 static outlet pressure of $p_{out} = 0.1 \text{ MPa}$ and the varying
385 opening angle ϕ . The boundary conditions at the inlet
386 and outlet also included the turbulent quantities, which
387 in this study were the turbulence intensity of 2% and
388 the turbulence length scale, the hydraulic diameter of
389 the inlet and outlet.

390 3.5. Oil model

391 The oil used in the CFD study is the petroleum-based
392 anti-wear hydraulic mineral oil, viscosity grade 32. It
393 has been treated as a compressible fluid, i.e. viscosity-
394 and density-temperature functions were used by the
395 FloEFD solver, although the temperature increase has
396 been proven to be local in small areas next to the
397 throttling edges [31].

398 The temperature field in the fluid subdomain is
399 non-uniform. The initial oil temperature was taken

400 equal to 45°C that corresponded to normal operational
401 conditions of fluid power systems as well as intended
402 test conditions. Oil properties correlating to this value
403 of oil temperature [32] as well as other preprocessing
404 settings of the CFD model are summarized in table 1.

405 3.6. Modelling results

406 3.6.1. Metering characteristic

407 During the CFD simulation studies of the valve, the
408 spool angular position is considered as the main
409 geometric parameter ranging from $\phi = 10^\circ$ to 90°
410 with an increment of 5° . The pressure drop across the orifice
411 had definite values of $\Delta p = 0.25 \text{ MPa}$, 0.5 MPa and
412 1 MPa . The volume flow rate $Q_{CFD}(\phi)$ as a function of
413 the spool position has been simulated for the specified
414 pressure drops. Interpolated plots for discrete data
415 points of CFD calculated flow rates are illustrated in
416 fig. 7.

417 The CFD simulated volume flow rate Q_{CFD} increases
418 non linearly as the orifice area grows. From $\phi = 25^\circ$
419 to 60° of the spool angular position the volume flow
420 rate exhibits steeper rise comparing with the regions of
421 extreme spool positions. According to the simulated

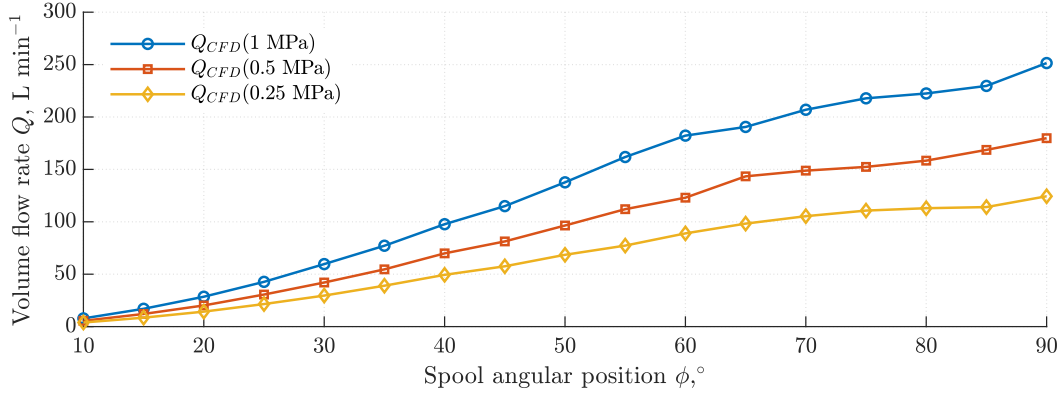


Figure 7: Modelled metering characteristic $Q(\phi)$ at $\Delta p = 0.25; 0.5; 1 \text{ MPa}$

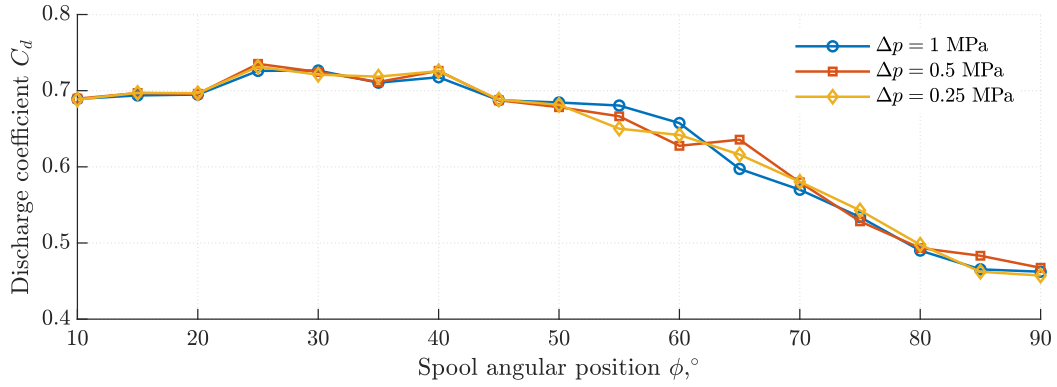


Figure 8: Discharge coefficient $C_d(\phi)$ at $\Delta p = 0.25; 0.5; 1 \text{ MPa}$

422 results, domains close to the maximum and minimum
 423 spool positions have more gradual flow rate gains. This
 424 benefits controllability of a hydraulic actuator at small
 425 and maximum speed regimes.

426 3.6.2. Discharge coefficient

427 Simulated flow rate characteristic Q_{CFD} of the valve has
 428 allowed calculation of the discharge coefficient of the
 429 orifice for any given spool angular position according
 430 to the Bernoulli equation.

$$431 C_d(\phi) = \frac{Q_{CFD}}{A(\phi)} \sqrt{\frac{\rho}{2\Delta p}} \quad (14)$$

432 For every pressure drop across the valve, computed
 433 discharge coefficient curves in fig. 8 follow the same
 434 trend and effectively coincide. Regardless of the
 435 imposed pressure differentials, discharge coefficient
 436 curves decrease as the valve opens. The maximum value
 of the coefficient is $C_{d,max} = 0.735$ at $\phi = 25^\circ$, the

437 minimal value is $C_{d,min} = 0.457$ at the valve's open
 438 state, $\phi = 90^\circ$. With the predetermined orifice area and
 439 the discharge coefficient relation, hydraulic behaviour
 440 of the valve can be predicted for any operational regime
 441 of the hydraulic system.

442 3.6.3. Reynolds number

443 To confirm the turbulent nature of an oil flow pattern
 444 in the valve for different spool angular positions,
 445 estimation of the Reynolds number Re has been
 446 performed according to the equations below:

$$447 Re = \frac{\rho VL}{\mu} = \frac{VL}{\nu} \quad (15)$$

448 where V and L are characteristic velocity and length
 449 scales of the flow, ρ , μ and ν – fluid's density, dynamic
 and kinematic viscosity respectively, [33].

450 For circular conduits, the Reynolds number can be
 451 expressed through the volume flow rate Q , the flow area

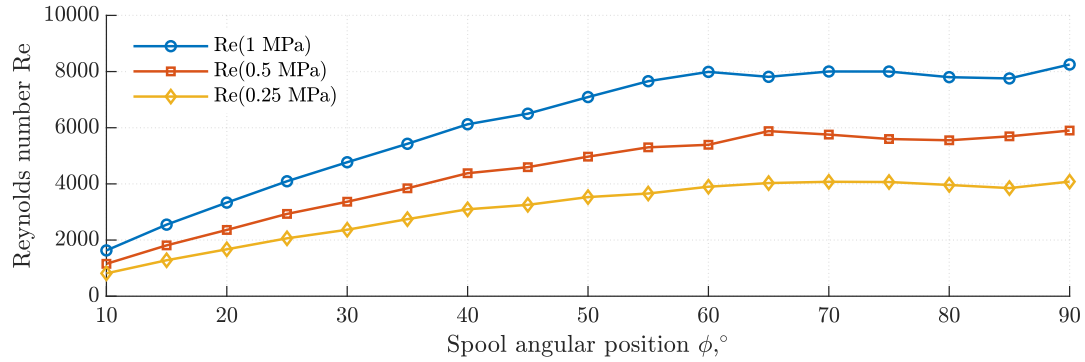


Figure 9: Reynolds number function $Re(\Delta p, \phi)$

452 A and the hydraulic diameter D_h , which is the same as
 453 the pipe diameter or the characteristic length L , [34].
 454 The more general formula for the hydraulic diameter,
 455 which accounts for noncircular pipes and hoses as the
 456 drop-shaped orifice, is

$$D_h = \frac{4A}{S} \quad (16)$$

457 where S is the perimeter of the flow cross-section. For
 458 the case of the initially chosen drop-shaped orifices, the
 459 total orifice perimeter S and area A were measured. The
 460 results are demonstrated in figs. 3 and 4 respectively.
 461 Therefore, it was possible to calculate the hydraulic
 462 diameter D_h of the orifice and use it further to estimate
 463 the Reynolds number.

464 The formula used for Reynolds number estimation is
 465 derived from eq. (15) through the hydraulic diameter D_h
 466 in eq. (16), the volume flow rate Q passing through the
 467 area A .

$$Re = \frac{QD_h}{Av} \quad (17)$$

468 The results of the Reynolds number calculations for
 469 different pressure differentials Δp and spool angular
 470 positions ϕ are illustrated in fig. 9. The figure confirms,
 471 that for considered values of the valve opening and
 472 the pressure differential, the valve operates with the
 473 turbulent flow pattern since the Reynolds number
 474 exceeds the critical value of 2300 at almost all simulated
 475 design points.

476 It also can be concluded, that in the range of small valve
 477 openings, when the spool is positioned at $\phi < 30^\circ$, the
 478 flow can take transitional nature in the throttling orifice
 479 areas as in this band the Reynolds number is within
 480 $1000 < Re < 4800$.

3.6.4. Pressure losses

481 In order to estimate the pressure loss p_{loss} imposed by
 482 the valve on the hydraulic circuit that the valve had
 483 been installed into, the volume flow rate Q passing
 484 through the valve and the outlet pressure of 0.1 MPa
 485 were selected as the hydraulic boundary conditions. The
 486 volume flow rate varied in a range $Q = 25 \text{ L min}^{-1}$ to
 487 275 L min^{-1} . The spool angular position ranges as $\phi =$
 488 40° to 90° . The measured goal is the magnitude of inlet
 489 pressure p_{in} . Hence, the pressure loss is defined by the
 490 difference
 491

$$p_{loss} = p_{in} - p_{out}. \quad (18)$$

492 The resultant pressure loss curves, i.e. $p_{loss}(Q)$ at
 493 $\phi = \text{const}$, for specified flow rates increase nonlinearly,
 494 with the dependency close to exponential. The
 495 maximum p_{loss} does not exceed 1 MPa at the fully open
 496 state of the valve and the maximum flow rate through it,
 497 i.e. at $Q(\phi_{max})$, see fig. 10.

$$P_{loss} = p_{loss}Q. \quad (19)$$

498 The obtained pressure loss function $p_{loss}(Q)$ allows
 499 further calculation of the power losses due throttling,
 500 see fig. 11, according to the formula below. This power
 501 is dissipated through oil viscous friction and increases
 502 the internal energy of the oil [1].

4. Experimental study

503 A prototype of the valve was manufactured in order to
 504 test and validate the theoretical model of the valve
 505 described above. A detailed experimental procedure is
 506 designed to test the behaviour of the valve within the
 507 hydraulic system and test its modelling characteristics.
 508

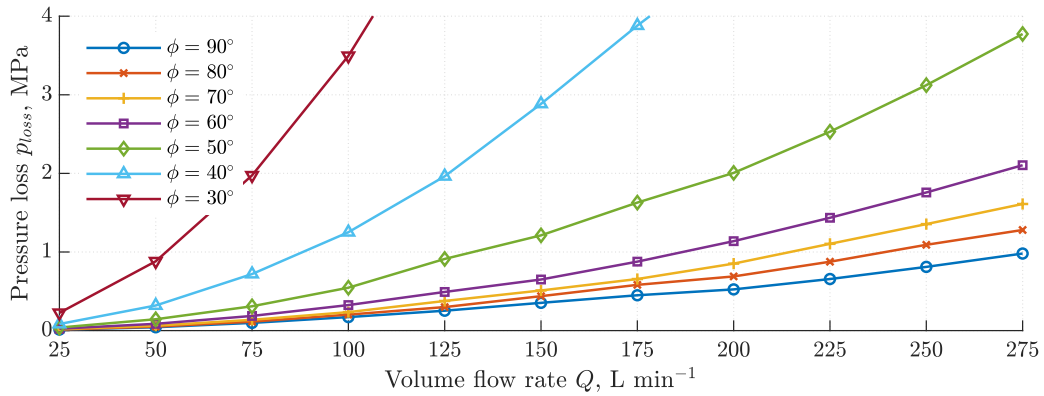


Figure 10: Modelled pressure losses $p_{loss}(Q)$ at $\phi = \text{const.}$

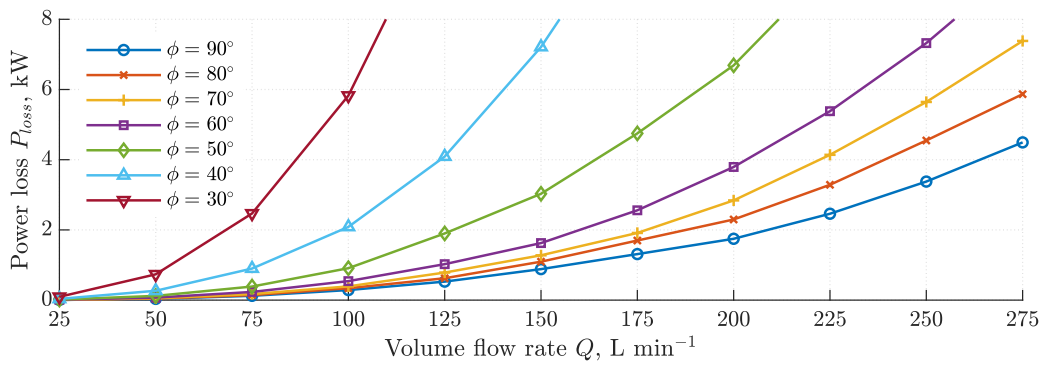


Figure 11: Modelled power losses $P_{loss}(Q)$ at $\phi = \text{const.}$

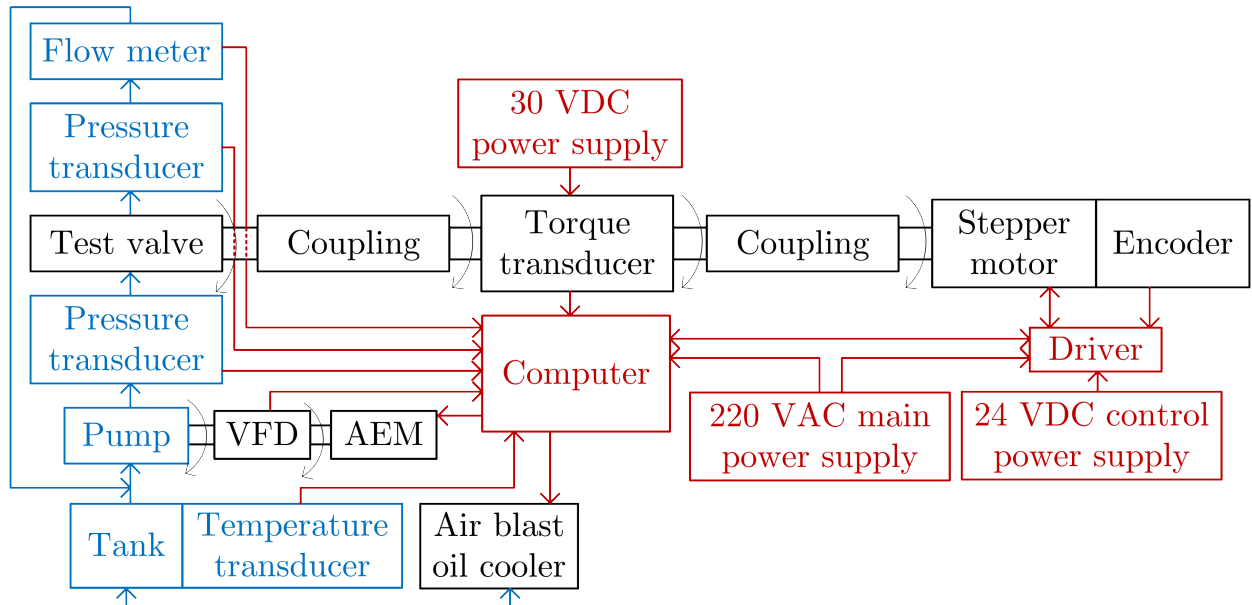


Figure 12: The block scheme of the data acquisition system. Blocks and signals colors correspond to: black – mechanical, blue – hydraulic, red – electric.

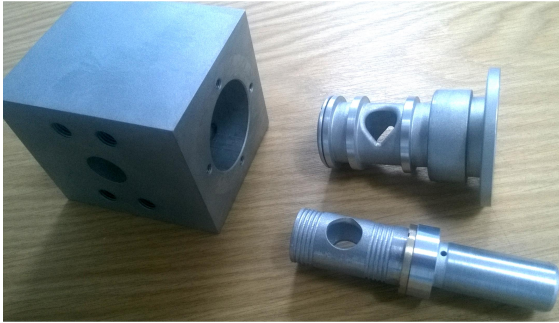


Figure 13: The main manufactured parts of the prototype valve: the valve body, the guiding sleeve inside the main sleeve, the spool with the thrust bearing on it.

543 mechanical component was described in the preceding
 544 sections. The details of the hydraulic test bench are
 545 discussed in the following section. Depending on the
 546 characteristic of interest, the monitored and controlled
 547 variables varied. Exact sets of monitored and controlled
 548 variable are summarized in the following experiment
 549 description.

509 4.1. Prototype valve

510 A physical prototype of the valve was manufactured
 511 by a contractor and assembled in accordance with
 512 the design specification described in section 2. The
 513 prototype valve comprised original, standard and
 514 “off-the-shelf” parts.

515 Original parts include the RTSV’s mechanical parts
 516 required to execute the new throttling method. These
 517 were manufactured in accordance with the design
 518 described above, see fig. 13.

519 However, a few geometrical simplifications of the
 520 valve parts were applied. Although the valve body’s
 521 collecting channel in the prototype had a rectangular
 522 cross-section area A_{an} , the area was kept the same
 523 as in the original design specification, where the
 524 channel’s shape corresponds to the one illustrated in
 525 fig. 1. Transition from the collecting channel to
 526 the outlet hydraulic port did not have a fillet on it.
 527 These deviations were considered as negligible and not
 528 influencing the overall valve performance. The overall
 529 length of the body was slightly shortened to reduce
 530 amount of the needed material. This resulted in small
 531 offset in the mounting threaded holes, which was taken
 532 into account during designing of the mounting base
 533 plate assembly described below.

534 4.2. Data acquisition system

535 The experimental data acquisition system (DAS) was
 536 used to collect data about the behaviour of the new valve
 537 in physical environment, as a part of a hydraulic system.
 538 The main purpose of the used DAS is to enable safe
 539 collection of the test data since the main component of
 540 the hydraulic is the mineral oil under high pressure.

541 DAS can be divided into three parts according to the
 542 physical nature of transmitted signals, see fig. 12. The

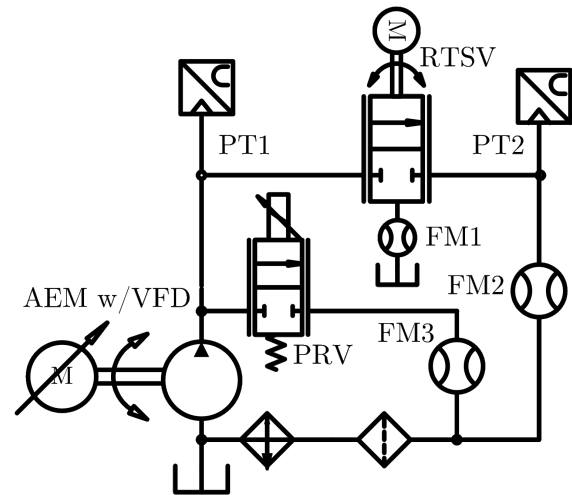
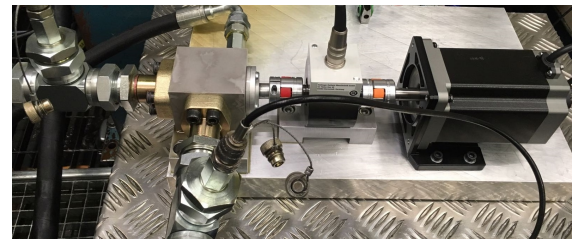
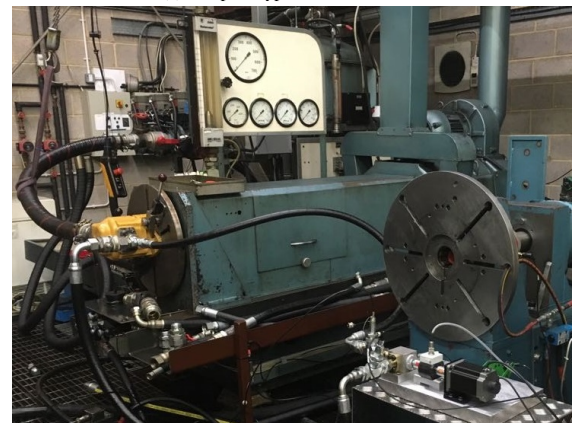


Figure 14: The scheme of the hydraulic test rig.



(a) The prototype valve, the RTSV.



(b) The hydraulic test rig.

Figure 15: The photos of the used hydraulic test rig.

Instrument	Make	Model	Range	Accuracy
Pump	Hydreco	QR6 6160	Displacement 160 cm ³ rev ⁻¹ Speed 450 rev min ⁻¹ to 2750 rev min ⁻¹	
FM	Kracht	VC12	2 L min ⁻¹ to 600 L min ⁻¹ Resolution 83.33 impulse rev ⁻¹ Tooth volume 12 cm ³	±0.3%
PT	Gems	3100B0400	400 bar Output 0.5 V to 4.5 V 4 mA to 20 mA	±0.25%
TT	HBM	T20WN	10 N m Output ±5 V 10 mA ± 8 mA	±0.5%
SM	Oriental Motors	RKS5913R	0.72° step	±0.05°

Table 2: Instrumentation.

4.2.1. Hydraulic test rig

Figure 14 shows the scheme of the hydraulic test setup used for the experiments. It can be divided on the power, oil conditioning subsystems, sensors and the test prototype valve, RTSV. Figure 15a shows specifically the prototype valve, RTSV, and fig. 15b illustrates the general view on the used test rig.

The oil storing and conditioning subsystem included an oil tank with an inbuilt heater, oil filters, and an air blast heat exchanger. The tank also comprised a breather that connected the tank's chamber to surrounding environment to ensure that the atmospheric pressure level was maintained in the tank and the return line of the hydraulic system.

The power subsystem of the test rig was equipped with an asynchronous electric motor (AEM) with a variable frequency drive (VFD). The AEM served as a pump's driver, while the VFD allowed to set the rotational speed of the pump's shaft and, hence, to control the pump's volume flow rate supplied into the hydraulic system. The pump used here was a Hydreco's spur gear pump QR6 series with displacement of 160 cm³ rev⁻¹, see the yellow-painted element in fig. 15b. Its operating speed range is 450 rev min⁻¹ to 2750 rev min⁻¹, [35].

In the power subsystem, in parallel to the pump, there was a pressure relief valve (PRV), which was installed in the by-pass line. The PRV is electronically controlled proportional valve, which allowed to set the valve's inlet pressure to the desired value. It also limited the pressure level in the hydraulic system, implementing the safety function. The by-pass line also included the flow meter FM3 to monitor the amount of flow passing through this line. The main hydraulic line incorporated the test valve, RTSV. The drain line of the RTSV featured the flow meter FM1 to measure the internal leak through the valve's parts. Up- and downstream to the prototype

valve, two pressure transducers were mounted PT1 and PT2 respectively. Additionally, the flow meter FM2 was installed in the downstream of the test line to enable measuring the volume flow rate passing through the test valve.

4.2.2. Instrumentation

The oil's supply subsystem allowed keeping the temperature level constant in time. Thermocouples, the air-blast oil cooler and the heater formed the closed-loop temperature control system. The tank-embedded thermocouples serving as temperature sensors allowed setting the temperature level on the same level throughout the length of an experiment. The working fluid was a zinc and chlorine free anti-wear hydraulic oil, Shell Tellus S2 V32 [36].

To monitor volume flow rates circulating the hydraulic system, three gear-type flow meters FM1, FM2 and FM3 were installed in the following hydraulic lines: pumps's by-pass, test valve's line and valve's internal leakage line. The latter enabled measurement of the oil spillage from the valve's central chamber, through the spool-sleeve gap and the thrust bearing to the tank. The leak drain line allows to lubricate all mechanical contacts within the valve with the working fluid, collect the leakage flow and direct it to the tank, see fig. 1.

The flow meters included two non-contacting measuring gears, which were driven by the liquid flow on a principle of a gear pump [37]. The pressure transducers were used to collect the data related to static pressure. The pressure transducers feature a sputter diaphragm, deformation of which is sensed and transformed into the pressure signal [38].

The used instrumentation is summarized in table 2. According to the sensors' datasheets, accuracy of the used transducers can ensure low systematic errors.

Test	Variable	Type	Instrument	Range
$Q(\phi)$ at $\Delta p = \text{const}$	p_{in}	Controlled	VFD, PRV	0.35 MPa to 1.1 MPa
	ϕ	Controlled	SM	30° to 90°
	p_{out}	Monitored	PT2	40 MPa, see table 2
	Q	Monitored	FM2	600 L min ⁻¹ , see table 2
$\Delta p(Q)$ at $\phi = \text{const}$	Q	Controlled	VFD, PRV	25 L min ⁻¹ to 175 L min ⁻¹
	ϕ	Controlled	SM	50° to 90°
	p_{in}	Monitored	PT1	40 MPa, see table 2
	p_{out}	Monitored	PT2	40 MPa, see table 2

Table 3: Test plan.

4.3. Test procedures

The general goal during the design of the experiment stage was to replicate the valve metering characteristics obtained in the modelled environment. Test procedure development consisted of selecting and dividing the variables into controlled and recorded in order to enable recreation of the metering characteristics and pressure losses. The ranges of controlled variables corresponds to the boundary conditions used in the CFD parametric simulations for a particular metering function. The summary of the test procedure is listed in table 3. During all tests the oil temperature was kept constant at 45 °C.

4.4. Tests results

The following sections report the results of the experiments conducted as a part of this investigation. The data collection was performed in according to the test plan, see table 3. The figures shown below are the results of the static hydraulic representation of the proposed rotary flow control valve.

As a general note, visual inspection of the valve before, during and after each test did not reveal any leakages or visible deformations of the valve's parts. There were also no signs of rubber O-rings extrusions. The inspection allowed to conclude, that the valve was able to withstand highly pressurized oil without leakages and failure to operate. Therefore, the general design of the prototype was considered satisfactory and able to performs its functions.

4.4.1. Metering characteristic

During measurements of the volume flow rate characteristic of the valve $Q(\phi)$, the spool angular position was ranging from $\phi = 30^\circ$ to 90° . At every spool position ϕ , the PRV and the VFD were used to set the pressure differential across the valve equal to the values of $\Delta p = 0.25$ MPa, 0.5 MPa and 1 MPa. Then,

the readings from the flow meter on the main line were recorded.

Experimental graphs of the volume flow rate as a function of the spool angular position are shown in fig. 16. These follow the same trend as the CFD modelled one, see fig. 7. However, the magnitudes differ drastically, especially for small valve openings and the low-opening spool positions, i.e. up to $\phi = 30^\circ$, see fig. 17 showing the error between simulated and measured data.

According to fig. 17, the predicted values of the volume flow rate exceed the measured values by 48.75%, 51.77% and 55.85% in average for the three pressure drops of 1 MPa, 0.5 MPa and 0.25 MPa respectively. The error between the measured, see fig. 16, and modelled, see fig. 7, volume flow rates does not depend on the pressure drop causing the flow. That testifies to consistent data collection.

4.4.2. Pressure losses

During measurements of the pressure losses, VFD and PRV were simultaneously used to control the pump's discharge volume flow rate and the valve's inlet pressure respectively. The spool was put in the predetermined position in the range $\phi = 50^\circ$ to 90° according to the test procedure. The spool openings below $\phi = 50^\circ$ caused the inlet pressure to rise above 20 MPa, which was considered unsafe. The parameters monitored were the valve's outlet and inlet pressure levels. The difference between these values constituted the predicted pressure drop Δp , or the pressure loss.

The opposite tendency to the volume flow rate results was observed to the pressure drop curves. Here, the experimental values are higher than the modelled with a higher similar margin. The pressure measurements were performed with the maximum volume flow rate 175 L min⁻¹. Further increase in the volume flow rate led to the inlet pressure level rise above 20 MPa, which

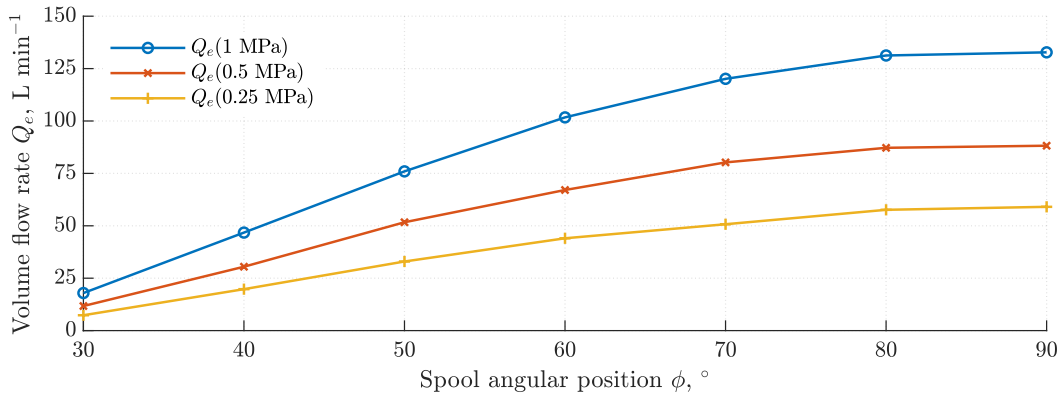


Figure 16: Tested metering characteristic $Q_e(\phi)$ at $\Delta p = 0.25; 0.5; 1 \text{ MPa}$

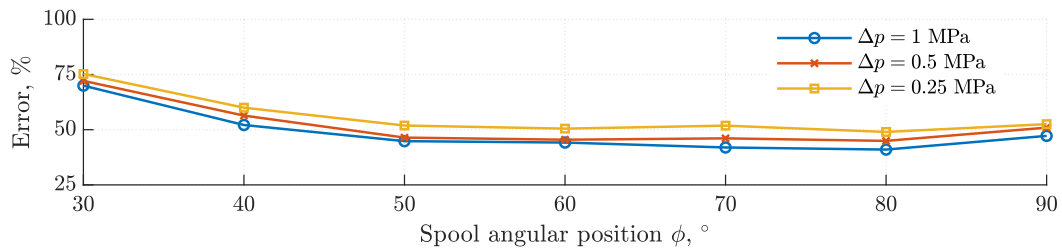


Figure 17: Percentage difference between simulated and tested metering characteristic $Q(\phi)$ at $\Delta p = 0.25; 0.5; 1 \text{ MPa}$

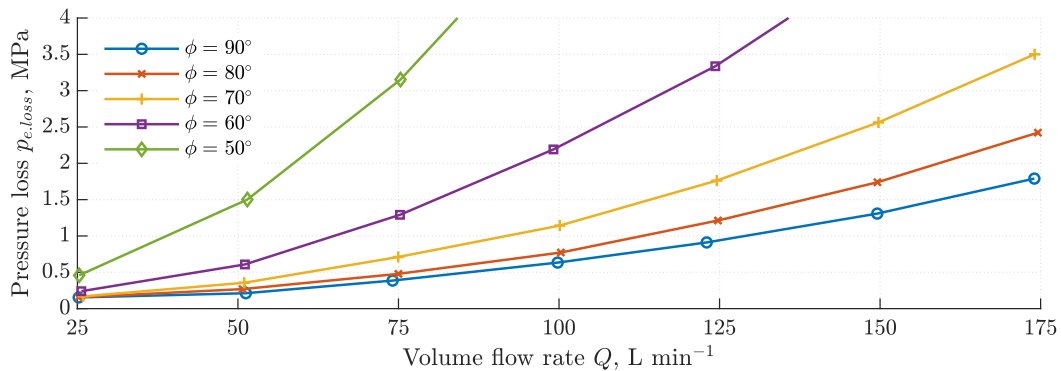


Figure 18: Tested pressure loss $p_{e.loss}$ at $\phi = \text{const.}$

694 was considered risky in terms of structural integrity of
695 the valve.

696 In case of pressure drop measurements, the simulated
697 results, see fig. 10, and the test results, see fig. 18,
698 differ, see the percentage differences between the two
699 for certain valve openings in fig. 19. The smaller valve
700 openings result in the highest results error of 90.25%
701 on average, i.e. in these cases experimental results are
702 almost two times bigger than simulated, regardless of
703 volume flow rate.

704 As the opening reaches maximum, the error decreases
705 reaching 72.69% in the range of volume flow rates from
706 100 L min⁻¹ to 150 L min⁻¹. At the fully open state and
707 the minimal volume flow rate, the error is comparable
708 with small opening's errors, i.e. 91.68%.

709 4.4.3. Correlation with modelling

710 According to figs. 17 and 19, the used simulation
711 model overestimates the performance characteristics of
712 the physical prototype valve for both the volume flow

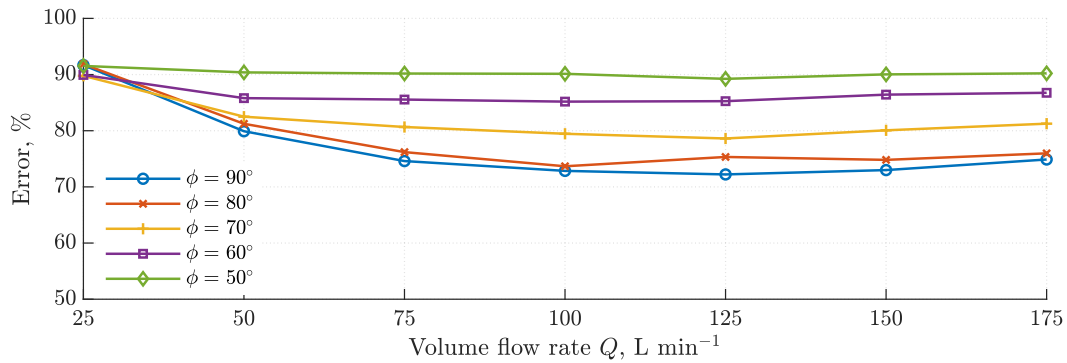


Figure 19: Percentage difference between modelled and tested pressure drops $\Delta p(Q)$ at $\phi = \text{const.}$

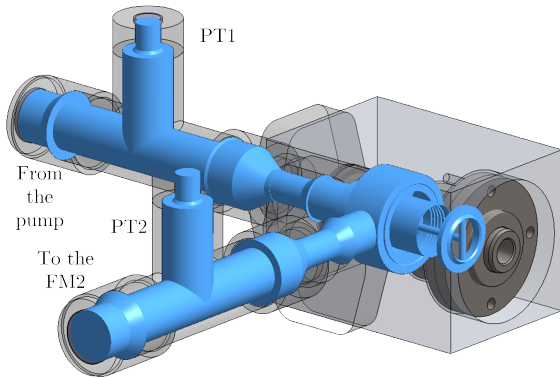


Figure 20: Corrected geometric model and fluid sub domain.

713 rate and the pressure drop curves. For the pressure
 714 drop the deviation reaches on average 82.78%, see
 715 fig. 19. Nevertheless, general trends of the simulated
 716 and experimental results conform. In particular, the
 717 monotonous increase of the volume flow rate with valve
 718 opening for different values of constant pressure drops
 719 was observed, see figs. 7 and 16 for the simulated and
 720 experimental flow rate curves respectively. The pressure
 721 drops for a set value of the valve opening were raising
 722 with a volume flow rate growth, see fig. 10 for the
 723 numerical results and fig. 18 for the experimental.

724 Several factors were identified, which were causing
 725 such large errors. One factor affecting all measurements
 726 and all performed tests was related to the accuracy
 727 of the spool angular positioning. The prototype was
 728 assembled in a way that overlap angles at the closed
 729 state were impossible to measure and control. Hence,
 730 although the valve was closed, the exact lengths of the
 731 leak channels were hard to establish. Therefore, it was
 732 challenging to ensure that leak channels' lengths are
 733 equal to those used in the modelling stage. As a result,

734 the actual “zero” position differed from the simulated.
 735 In addition, a signal noise caused by the high variability
 736 of the flow parameters in time and non-uniformity of the
 737 pump's flow rate also affects the quality of the collected
 738 data due to introduction of a random error.

739 However, the main reason of the tested and modelled
 740 results differences can be attributed to the imperfections
 741 of the geometric model used. Firstly, it did not include
 742 fittings into the model's geometry. These fittings
 743 connect the pressure transducers and the prototype
 744 valve to the hydraulic system. Their internal passages
 745 were non-uniform in a cross-section, their routes were
 746 not straight. Hence, their internal passages created
 747 additional disturbances to the flow, which were not
 748 accounted in the simulation model. This is the
 749 first factor causing a divergence of the modelled and
 750 experimental valve's metering characteristics.

751 Moreover, the simulated geometric model did not
 752 take into account surfaces roughness of mechanical
 753 parts wetted with oil. Surface's roughness creates
 754 additional pressure losses due to viscous and boundary
 755 layer-surface friction. Together, these two factors
 756 can explain the difference between experimental and
 757 simulated results. To test these assumptions, additional
 758 modelling was performed.

4.4.4. Corrected model

759 To test the assumptions made, an extra run of the
 760 hydraulic behaviour modelling was performed. In
 761 this simulation the geometric model was corrected
 762 to include the instrumentation's fittings, pressure
 763 transducers' ports and adapters, which served as
 764 transition from one internal nominal diameter to
 765 another, see fig. 20. These elements were created with
 766 the internal geometry as close as possible to those used
 767 in testing.
 768

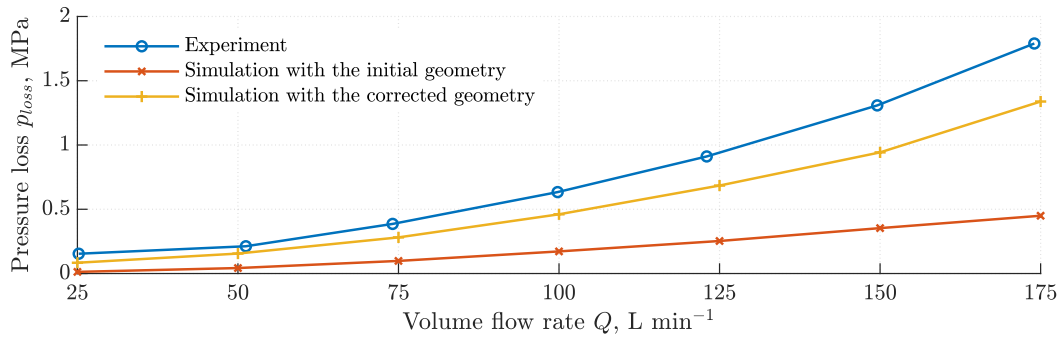


Figure 21: Correlation of study results for $\phi = 90^\circ$.

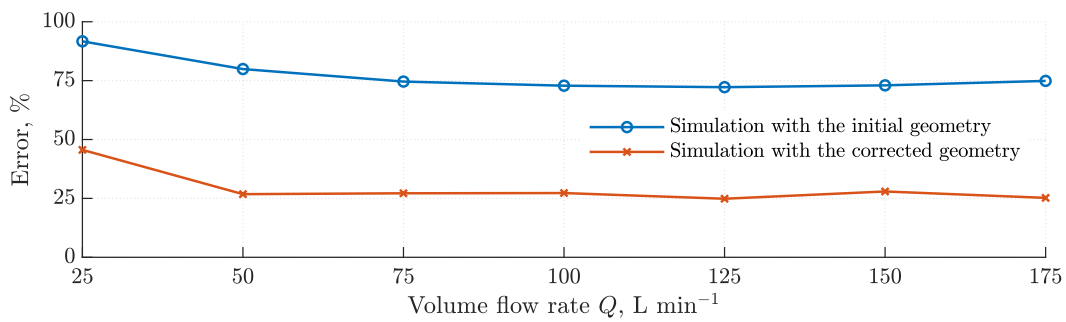


Figure 22: Percentage difference between simulated and test results of the pressure drop at $\phi = 90^\circ$ relatively to the experiment data after inclusion of the test rig elements.

769 To fully replicate the geometry of the tested prototype, 792
 770 the solid model of the valve has been modified as well. 793
 771 In the manufactured prototype the annular 794
 772 collecting channel had a rectangular shape without 795
 773 fillets. Similarly the spool and sleeve orifices in the 796
 774 test valve had right edges, with no fillets. According 797
 775 to these deviations of the valve internal geometry from 798
 776 the design specification, modifications of the body, 799
 777 the sleeve and the spool were introduced. Adopted 800
 778 geometrical corrections resulted in the modified 801
 779 flow path, which reflected the test conditions more 802
 780 accurately. 803

781 Furthermore, roughness of Ra_{25} was assigned to all 804
 782 internal surfaces and passages, which are in contact 805
 783 with oil. The chosen roughness corresponds to finishing 806
 784 levels of the manufacturing processes used during 807
 785 prototype production – metal cutting with rough finish. 808

786 To study the influence of the corrected geometry on the 809
 787 pressure drop, the hydraulic problem with the following 810
 788 boundary conditions was solved: the spool angular 811
 789 position $\phi = 90^\circ$, the volume flow rate range $Q =$ 812
 790 25 L min^{-1} to 175 L min^{-1} and the the outlet static 813
 791 pressure $p_{out} = 0.101 \text{ 325 MPa}$, the measured variable 814

is the inlet pressure p_{in} . Then, the pressure difference Δp was calculated and plotted, see fig. 21.

According to fig. 21, correcting the geometric model of the prototype valve brought the simulation results much closer to the experiment results. Taken measures to modify simulations allowed to reduce the average error between modelling and experiment by 47.75%, from 77.02% to 29.27%, see fig. 22. Therefore, it can be concluded that the biggest factor contributing to the simulation and the experiment results deviations was caused by the incomplete geometric model and the “smooth wall” assumption.

After introduced modifications to the CFD settings (inclusion of the fittings to the valve geometric model and adding roughness to the internal surfaces), the percentage difference between the corrected simulation and the experimental results still remained quite large, average 29.27%, see fig. 22. Despite this error, the applied simulation model can be considered accurate enough to predict hydraulic behaviour of the tested prototype valve. The simulation results from the previous chapters can be deemed valid too and used in further performance improvement, design optimization,

815 etc. The obtained metering characteristics from CFD 861
816 modelling hold their relevance since they pertained to 862
817 the valve geometry only, excluding the elements of the 863
818 hydraulic test rig and used instrumentation. 864

819 **5. Benchmark**

820 As a benchmark valve, Tecnord's products were 866
821 selected as the company is one of market leaders 867
822 in hydraulic components design and production. 868
823 Moreover, Tecnord's manual rotary spool valves 869
824 SJ-MRA [39] represent the closest analogue to the 870
825 developed valve both structurally and in terms of 871
826 specification. 872

827 According to the data sheet, the valve is a two ways, 875
828 two positions, proportional cartridge flow control valve 876
829 with a rotary, tubular spool, see fig. 23. It has a 877
830 cartridge-nest assembly method, the valve includes the 878
831 movable hollow spool inside the static sleeve as the 879
832 main throttling pair. The outside diameter of the sleeve 880
833 in this valve is determined by the thread 1'' 5/16, 881
834 which corresponds to 32 mm. The same outer sleeve 882
835 diameter in the developed RTSV is 29.51 mm. The 883
836 spool has two orifices, which are located opposite to 884
837 each other. Its nominal volume flow rate is 151 L min^{-1} , 885
838 the rated operational pressure is 20.7 MPa. Despite 886
839 many similarities, the Tecnord's valve is manually 887
840 driven, which substantially limits its ability for fine 888
841 control and, hence, its application range. 889

842 According to the performance data of this valve, in the 890
843 fully open state at the rated flow rate of 150 L min^{-1} the 891
844 created pressure drop by the valve makes up 1.1 MPa. 892
845 Whereas in the RTSV the corresponding pressure drop 893
846 constitutes 0.35 MPa, see fig. 10, with 67.9% difference 894
847 relatively to the Tecnord's valve. In this comparison, 895
848 the simulated data for the valve geometry without the 896
849 elements belonging to the test rig instrumentation was 897
850 used. The comparison results are illustrated in fig. 25. 898

851 The calculated percentage of the average pressure drop 899
852 reduction of 71.66% can be directly translated into 900
853 the energy efficiency gain. Since the throttling power 901
854 loss is proportional to the pressure drop, the curve 902
855 in fig. 25 also corresponds to percentage of efficiency 903
856 improvement relative to the Tecnord's reference valve. 904

857 **6. Discussion**

858 The performance evaluations during testing of the 905
859 new valve, referred as the Rotary Tubular-Spool Valve 906
860 (RTSV), allowed to validate the numerical models. The 907
908

861 simulated performance characteristics of the valve agree 862
863 well with experiments. The metering and pressure loss 864
865 functions were derived from CFD modelling and tested. 866
867 Therefore, the models could be further used to analyse 868
869 other aspects of RTSV's functionality. 870

871 The simulation results confirmed that the developed 872
873 RTSV can successfully perform the required functions 874
875 of a flow control valve in hydraulic systems and, thereby 876
877 control the speed of an actuator or a rotary hydraulic 878
879 motor. 880

881 Although the benchmark performance comparison 882
883 study showed significant increase in energy efficiency of 884
885 the new valve, it can differ for other valves designed by 886
887 other manufacturers. Nevertheless, the obtained results 888
889 confirm the potential of the new valve to become the 890
891 industry standard, to replace single-spool valves with 892
893 the independent metering arrangement of RTSVs to 894
895 control the actuator's speed. 896

897 **7. Conclusion**

898 The objective of this research was met by investigating 899
900 the three-dimensional fluid dynamics of internal flows 901
902 within the valve to determine the initial metering 903
904 characteristics and pressure losses it creates. The 904
905 simulation results demonstrated RTSV's flow control 905
906 feasibility as well as its ability to operate in the 906
907 high-flow rate operational domain, with the volume flow 907
908 rate reaching 250 L min^{-1} at 1 MPa pressure differential. 908
909 At the fully open state and the rated volume flow rate, 909
910 valve's pressure drop was 0.81 MPa. Its performance 910
911 was deemed comparable with industry available valves 911
912 and having great potential to compete with benchmark 912
913 hydraulic components. 913

914 The experimental investigation focused on 914
915 characterising the RTSV's hydraulic performance. 915
916 The prototype valve was built according to the 916
917 suggested design concept. The test rig and the data 917
918 acquisition system were designed, its elements were 918
919 acquired and assembled. These enabled to replicate 919
920 simulation set-up and to collect data pertaining to 920
921 performance characteristics simulated before. 921

922 Manufacturing and testing of the prototype proved 922
923 its relative design simplicity, promising functional 923
924 performance, its strength and ease of manufacture and 924
925 operation. The results of tests, although differing from 925
926 initial simulations in average by 52.12% for the volume 926
927 flow rate function and by 82.78% for pressure drops, 927
928 followed same trends as the modelled. The factors 928
929 causing the error were identified. To address these 929

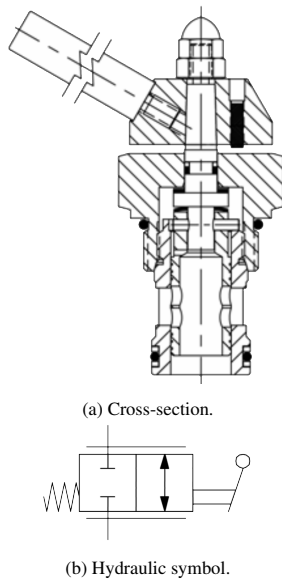


Figure 23: Tecnom's SJ-MRA rotary flow control valve, [39].

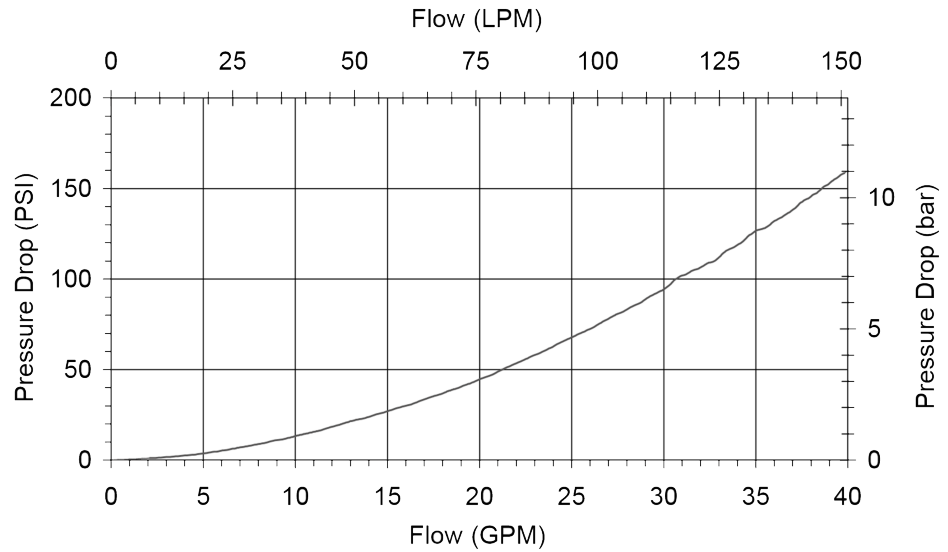


Figure 24: Test data of the pressure drop of SJ-MRA [39].

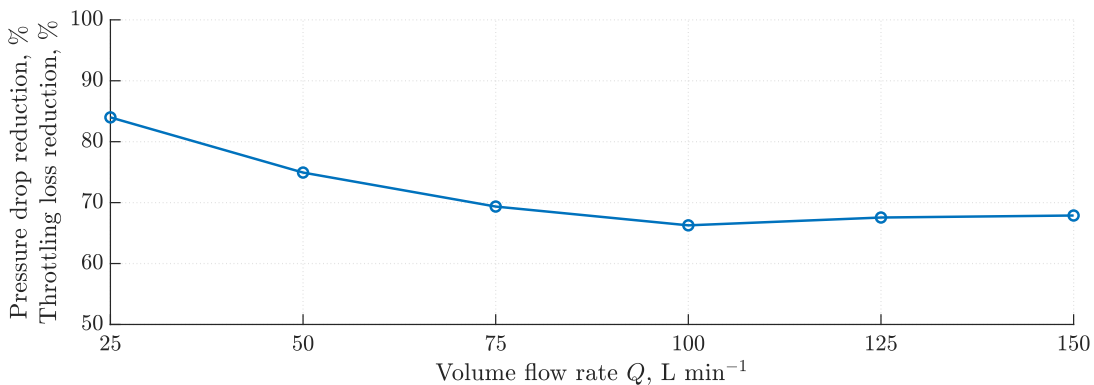


Figure 25: Throttling loss reduction in the RTSV relatively to the Tecnom's SJ-MRA.

909 factors, the CFD modelling settings were corrected. 923
 910 These corrections to the model significantly reduced 924
 911 simulation/experiment errors in average by 47.75% 925
 912 for the pressure drop function. Thereby the initial 926
 913 simulation results were validated. 927

914 The comparison study with the selected industrially 928
 915 available flow control valve having the similar structure 929
 916 and performance proved superior qualities of the 930
 917 developed RTSV. The ability of the novel valve to 931
 918 improve energy efficiency of hydraulic control system 932
 919 was demonstrated and thereby confirmed by evaluating 933
 920 and comparing throttling losses occurring in the RTSV 934
 921 and the reference valve. The average pressure drop 935
 922 reduction of the RTSV amounted to 71.66% relative to 936

923 the analogue valve. 924

924 References

- 925 [1] Merritt, Herbert E., Hydraulic Control Systems, John Wiley & Sons, Inc., New York, 1968.
- 926 [2] B. Eriksson, Mobile Fluid Power Systems Design with a Focus on Energy Efficiency, Doctoral dissertation, Linköping University (2010).
- 927 [3] C. Burrows, Fluid power—some reflections, in: The 6th International Conference on Hydraulic Machinery and Hydrodynamics, no. February, Timisoara, Romania, 2004, pp. 51–56.
- 928 [4] M. Axin, Mobile Working Hydraulic System Dynamics, Dissertation, Linköping University (2015).
- 929 [5] P. Tamburrano, A. Plummer, E. Distaso, R. Amirante, A review of direct drive proportional electrohydraulic spool valves: 930

- 938 Industrial state-of-the-art and research advancements, Journal 1003
939 of Dynamic Systems, Measurement and Control, Transactions 1004
940 of the ASME 141 (2). doi:10.1115/1.4041063. 1005
- 941 [6] N. Heraković, CFD simulation of flow force reduction in 1006
942 hydraulic valves, Tehnicki vjesnik - Technical Gazette 22 (2) 1007
943 (2015) 453–463. doi:10.17559/TV-20141128090939. 1008
- 944 [7] E. Lisowski, G. Filo, J. Rajda, Analysis of flow 1009
945 forces in the initial phase of throttle gap opening in 1010
946 a proportional control valve, Flow Measurement and 1011
947 Instrumentation 59 (2018) 157 – 167. doi:https://doi.org/10.1016/j.flowmeasinst.2017.12.011. 1012
948 URL [http://www.sciencedirect.com/science/](http://www.sciencedirect.com/science/article/pii/S095559861730331X) 1013
949 [article/pii/S095559861730331X](http://www.sciencedirect.com/science/article/pii/S095559861730331X) 1014
- 950 [8] E. Lisowski, W. Czyzycki, J. Rajda, Three dimensional CFD 1015
951 analysis and experimental test of flow force acting on the 1016
952 spool of solenoid operated directional control valve, Energy 1017
953 Conversion and Management 70 (2013) 220–229. doi:10.1016/j.enconman.2013.02.016. 1018
954 1019
- 955 [9] M. Rabie, Fluid Power Engineering, McGraw-Hill Education, 1020
956 2009. 1021
- 957 [10] J. Yu, J. Zhuang, D. Yu, Modeling and analysis of a rotary direct 1022
958 drive servovalve, Chinese Journal of Mechanical Engineering 1023
959 27 (5) (2014) 1064–1074. doi:10.3901/CJME.2014.0725. 1024
960 127. 1025
961 URL <https://doi.org/10.3901/CJME.2014.0725.127> 1026
962 1027
- 963 [11] H. Wang, G. Gong, H. Zhou, W. Wang, Steady flow torques in 1028
964 a servo motor operated rotary directional control valve, Energy 1029
965 Conversion and Management 112 (2016) 1–10. doi:10.1016/j.enconman.2015.11.054. 1030
966 1031
- 967 [12] M. Zhu, S. Zhao, J. Li, Design and analysis of a new high 1032
968 frequency double-servo direct drive rotary valve, Frontiers of 1033
969 Mechanical Engineering 11 (4) (2016) 344–350. doi:10.1007/s11465-016-0406-x. 1034
970 1035
971 URL <https://doi.org/10.1007/s11465-016-0406-x> 1036
972 1037
- 973 [13] M. Zhu, S. Zhao, P. Dong, J. Li, Design and analysis of a novel 1038
974 double-servo direct drive rotary valve with high frequency, 1039
975 Journal of Mechanical Science and Technology 32 (9) (2018) 1040
976 4313–4323. doi:10.1007/s12206-018-0829-x. 1041
977 URL <https://doi.org/10.1007/s12206-018-0829-x> 1042
- 978 [14] E. Husley, Rotary control valve, US3135293A (1962). 1043
- 979 [15] R. Erwin, E. Husley, Rotary sleeve valves, US3005468A (1958). 1044
- 980 [16] P. Bordovsky, K. Scmitz, H. Murrenhoff, CFD Simulation and 1045
981 Measurement of Flow Forces Acting on a Spool Valve, in: 1046
982 10th International Fluid Power Conference, Dresden, Germany, 1047
983 2016, pp. 473–484. 1048
- 984 [17] E. Lisowski, G. Filo, CFD analysis of the characteristics of 1049
985 a proportional flow control valve with an innovative opening 1050
986 shape, Energy Conversion and Management 123 (2016) 15–28. 1051
987 doi:10.1016/j.enconman.2016.06.025. 1052
- 988 [18] M. Zhu, S. Zhao, J. Li, P. Dong, Computational fluid dynamics 1053
989 and experimental analysis on flow rate and torques of a servo 1054
990 direct drive rotary control valve, Proceedings of the Institution 1055
991 of Mechanical Engineers, Part C: Journal of Mechanical 1056
992 Engineering Sciencedoi:10.1177/0954406218756449. 1057
- 993 [19] Ivan Okhotnikov, Siamak Noroozi, Philip Sewell, Philip 1058
994 Godfrey, Evaluation of steady flow torques and pressure losses 1059
995 in a rotary flow control valve by means of computational 1060
996 fluid dynamics, International Journal of Heat and Fluid Flow 1061
997 64 (2017) 89–102. doi:https://doi.org/10.1016/j.ijheatfluidflow.2017.02.005. 1062
- 998 [20] D. C. Wilcox, Turbulence Modeling for CFD, 3rd Edition, DCW 1063
999 Industries, Inc, 2006. 1064
- 1000 [21] SolidWorks, SolidWorks Flow Simulation (2015). 1065
- 1001 [22] A. Palumbo, R. Paoluzzi, M. Borghi, M. Milani, Forces on a 1066
1002 hydraulic valve spool, Proceedings of the JFPS International 1067
1068 Symposium on Fluid Power 1996 (3) (1996) 543–548. doi: 10.5739/isfp.1996.543. 1069
- [23] SolidWorks, Enhanced Turbulence Modeling in SolidWorks 1070
Flow Simulation (2013). 1071
- [24] C. K. G. Lam, K. Bremhorst, A Modified Form of the $k-\epsilon$ Model 1072
for Predicting Wall Turbulence, Journal of Fluids Engineering 1073
103 (3). doi:10.1115/1.3240815. 1074
- [25] A. Sobachkin, G. Dumnov, Numerical Basis of CAD-Embedded 1075
CFD, NAFEMS World Congress 2013 February (2013) 1–20. 1076
- [26] Launder, B.E. E. and Spalding, D.B. B., The numerical 1077
computation of turbulent flows, Computer Methods in Applied 1078
Mechanics and Engineering 3 (2) (1974) 269–289. 1079
- [27] E. R. V. Driest, On Turbulent Flow Near a Wall, Journal of 1080
the Aeronautical Sciences 23 (11) (1956) 1007–1011. doi: 10.2514/8.3713. 1081
- [28] SolidWorks, Advanced Boundary Cartesian Meshing 1082
Technology in SolidWorks Flow Simulation (2013). 1083
- [29] T. Dell, Load-Sensing Pressure-Compensating (LSPC) 1084
Hydraulic Systems, in: Hydraulic Systems for Mobile 1085
Equipment, Goodheart-Willcox, 2017, Ch. 18. 1086
- [30] B. Nielsen, Controller Development for a Separate Meter-In 1087
Separate Meter-Out Fluid Power Valve for Mobile Applications, 1088
Ph.D. thesis, Aalborg University (2005). 1089
- [31] H. Ji, Y. Cao, Z. Wang, Y. Wang, Numerical analysis of 1090
temperature rise by throttling and deformation in spool valve, 1091
Proceedings of 2011 International Conference on Fluid Power 1092
and Mechatronics, FPM 2011 (2011) 752–756doi:10.1109/FPM.2011.6045861. 1093
- [32] CITGO, Product Information. CITGO A/W Hydraulic oils 1094
(2015). 1095
- [33] F. White, Fluid Mechanics, the fourth Edition, McGraw-Hill 1096
series in mechanical engineering, 1999. 1097
- [34] W. Durfee, Z. Sun, Fluid Power System Dynamics, Center for 1098
Compact and Efficient Fluid Power (CCEFP), Department of 1099
Mechanical Engineering, University of Minnesota, 2009. 1100
- [35] Hydreco, Q Series Hydraulic Gear Pumps (2017). 1101
URL [https://www.hydreco.com/info-downloads/](https://www.hydreco.com/info-downloads/technical-data-sheets/) 1102
[technical-data-sheets/](https://www.hydreco.com/info-downloads/technical-data-sheets/) 1103
- [36] Shell, Industrial Hydraulics Fluid Shell Tellus S2 V32 (2017). 1104
URL <http://www.epc.shell.com/> 1105
- [37] Kracht, Gear Type Flow Meter VC (2017). 1106
URL [http://www.krachtcorp.com/wp-content/](http://www.krachtcorp.com/wp-content/uploads/2012/05/VC_USA_02-12_view.pdf) 1107
[uploads/2012/05/VC_USA_02-12_view.pdf](http://www.krachtcorp.com/wp-content/uploads/2012/05/VC_USA_02-12_view.pdf) 1108
- [38] Gems, 3100 Series and 3200 Heavy Duty Series Compact OEM 1109
Pressure Transmitters (2017). 1110
URL [https://www.gemssensors.co.uk/~media/](https://www.gemssensors.co.uk/~media/files/resources/na_english/catalogpages/catalog_h_3100series-3200series.ashx) 1111
[files/resources/na_english/catalogpages/](https://www.gemssensors.co.uk/~media/files/resources/na_english/catalogpages/catalog_h_3100series-3200series.ashx) 1112
[catalog_h_3100series-3200series.ashx](https://www.gemssensors.co.uk/~media/files/resources/na_english/catalogpages/catalog_h_3100series-3200series.ashx) 1113
- [39] Tecnod, SJ-MRA Manual Rotary Spool Valve, 2 Way (2017). 1114
URL [https://www.tecnord.com/tabelle/](https://www.tecnord.com/tabelle/cartridge-valves/mechanical-directional-pdf/SJ-MRA.pdf) 1115
[cartridge-valves/mechanical-directional-pdf/](https://www.tecnord.com/tabelle/cartridge-valves/mechanical-directional-pdf/SJ-MRA.pdf) 1116
[SJ-MRA.pdf](https://www.tecnord.com/tabelle/cartridge-valves/mechanical-directional-pdf/SJ-MRA.pdf) 1117